

# Power spectrum and Intermittency of the Transmitted Flux of QSOs' Ly $\alpha$ Absorption Spectra

Priya Jamkhedkar\*, Long-Long Feng<sup>†</sup>, Wei Zheng<sup>‡</sup>,  
David Kirkman<sup>§</sup>, David Tytler<sup>¶</sup>, Li-Zhi Fang<sup>||</sup>

## Abstract

Using a set of 28 high resolution, high signal to noise ratio (S/N) QSO Ly $\alpha$  absorption spectra, we investigate the non-Gaussian features of the transmitted flux fluctuations, and their effect upon the power spectrum of this field. We find that the spatial distribution of the local power of the transmitted flux on scales  $k \geq 0.05$  s/km is highly spiky or intermittent. The probability distribution functions (PDFs) of the local power are long-tailed. The power on small scales is dominated by small probability events, and consequently, the uncertainty in the power spectrum of the transmitted flux field is generally large. This uncertainty arises due to the slow convergence of an intermittent field to a Gaussian limit required by the central limit theorem (CLT). To reduce this uncertainty, it is common to estimate the error of the power spectrum by selecting subsamples with an “optimal” size. We show that this conventional method actually does not calculate the variance of the original intermittent field but of a Gaussian field. Based on the analysis of intermittency, we propose an algorithm to calculate the error. It is based on a bootstrap resampling among all independent local power modes. This estimation doesn't require any extra parameter like the size of the subsamples, and is sensitive to the intermittency of the fields. This method effectively reduces the uncertainty in the power spectrum when the number of independent modes matches the condition of the CLT convergence.

## 1 Introduction

Ly $\alpha$  absorption on the short wavelength side of Ly $\alpha$  emission in QSO spectra with high redshift indicates the presence of neutral hydrogen (HI) along the line of sight. The low column density ( $10^{13}$  to  $10^{17}$  cm $^{-2}$ ) HI absorption is believed to be due to diffusely distributed intergalactic medium (IGM). The IGM mass field is passive with respect to the dark matter present in the sense that its gravitational clustering is dominated by the gravity of dark matter. The IGM is assumed to be a good tracer of the underlying mass density distribution on scales larger than the thermal diffusion or Jeans length in the linear or even the nonlinear regime (Bi, 1993; Fang et al. 1993; Hui, & Gnedin 1997; Nusser, & Haehnelt 1999). The statistical features of the QSO Ly $\alpha$  transmitted flux can be used to estimate the corresponding features of the underlying mass field. Consequently, the power spectrum of the transmitted flux fluctuations of high redshift QSOs' Ly $\alpha$  absorption spectrum has been extensively used for reconstructing the initially linear perturbations of the cosmic mass and velocity fields and discriminating among models of structure formation (Bi, Ge, & Fang 1995; Bi, & Davidsen 1997; Croft et al. 1999, 2002; Feng, & Fang 2000; McDonald et al 2000; Pando, Feng & Fang 2001; Zhan, & Fang 2002).

Therefore, it is necessary to study the effects of the non-Gaussian features of the flux field upon the detection of the power spectrum of this field, and its error estimation. In this paper, we will focus on the effects of intermittency of the QSO Ly $\alpha$  transmitted flux on the power spectrum estimation.

\*Department of Physics, University of Arizona, Tucson, AZ 85721

<sup>†</sup>Center for Astrophysics, University of Science and Technology of China, Hefei, Anhui 230026, P. R. China, and National Astronomical Observatories Chinese Academy of Science, Chao-Yang District, Beijing 100012, P. R. China

<sup>‡</sup>Department of Physics and Astronomy, The Johns Hopkins University, Baltimore, MD 21218

<sup>§</sup>Center of Astrophysics and Astronomy, University of California, San Diego, CA 92093

<sup>¶</sup>Center of Astrophysics and Astronomy, University of California, San Diego, CA 92093

<sup>||</sup>Department of Physics, University of Arizona, Tucson, AZ 85721

The first indication of intermittency arises from the success of the lognormal model in explaining the QSO Ly $\alpha$  forests (Bi 1993; Bi, & Davidsen 1997) as a lognormal field typically is intermittent. To approximately describe the evolution of the IGM by a stochastic Burgers' equation, the IGM mass and velocity fields are found to be lognormal or intermittent (Jones, 1999; Matarrese, & Mohayaee 2002). Intermittency has been detected with high resolution, high signal to noise ratio (S/N) samples of QSO Ly $\alpha$  absorption spectra (Jamkhedkar, Zhan, & Fang 2000; Feng, Pando, & Fang 2001; Zhan, Jamkhedkar, & Fang 2001; Jamkhedkar 2002). Recently, the intermittent features have been further examined by measuring the structure function and intermittent exponent of 28 Keck HIRES QSO spectra (Pando et al. 2002). This work shows that the intermittent behaviour is significant on scales  $k > 0.05$  s/km.

A basic characteristic of an intermittent field is that the power of the fluctuations of the flux field is concentrated in rare spikes which are randomly and widely scattered in space, with low power between the spikes. In this case, the power spectrum of an intermittent field is dominated by rare and improbable events (spikes). In other words, only a small fraction of the total modes contribute to the power while most are inactive. Although an intermittent field is statistically homogeneous, the rare events lead to significant differences among samples from different parts of the universe when the spatial size of the region is not large enough to contain numerous spikes. Mathematically, this makes the central limit theorem less effective. All these imply that the uncertainty in the power spectrum is directly related to the intermittency of the field.

Using the same samples studied by Pando et al. (2002), we will investigate the uncertainty of the power spectrum of QSO Ly $\alpha$  transmitted flux fluctuations. The paper is organised as follows. §2 briefly introduces the basic properties of an intermittent field. §3 presents our algorithm for calculating the power spectra with the discrete wavelet transform (DWT). §4 describes the samples used for analysis. §5 discusses the basic properties of the DWT power spectrum of the samples. §6 addresses the effect of the intermittent behaviour upon the power spectrum. Finally, §7 summarises the results and conclusions.

## 2 Intermittent field

Most of this section has been presented in our previous work (Pando et al 2002). For the paper to be self-contained, we repeat these results very briefly. The principal characteristic of an intermittent random field, like Ly $\alpha$  transmitted flux  $F(\lambda)$ , is measured by the asymptotic behaviour of the ratio between the high- and low-order moments of the field defined as

$$\frac{\langle [F(x+r) - F(x)]^{2n} \rangle}{[\langle [F(x+r) - F(x)]^2 \rangle]^n} \asymp \left\langle \frac{r}{L} \right\rangle^\zeta, \quad (1)$$

where  $\langle \dots \rangle$  is the average over the ensemble of fields, and  $L$  is the size of the sample. Eq. (1) can be rewritten as

$$\frac{S_r^{2n}}{[S_r^2]^n} \propto \left( \frac{r}{L} \right)^\zeta, \quad (2)$$

where  $S_r^{2n}$  is the structure function defined by

$$S_r^{2n} = \langle |\Delta_r(x)|^{2n} \rangle. \quad (3)$$

Here  $\Delta_r(x) \equiv F(x+r) - F(x)$ .  $S_r^{2n}$  is the  $2n^{\text{th}}$  moment of the fluctuations of the field. Therefore, the ratio in eq. (2) is the  $2n^{\text{th}}$  moment  $S_r^{2n}$  normalised by the  $n^{\text{th}}$  power of the  $2^{\text{nd}}$  moment, or power,  $S_r^2$ .

A field is intermittent if the exponent  $\zeta$  is negative on small scales  $r$  (Gärtner, & Molchanov, 1990; Zel'dovich, Ruzmaikin, & Sokoloff, 1990). Intermittency is measured by the  $n$ - and  $r$ -dependencies of  $\zeta$ . For a Gaussian field,

$$\frac{S_r^{2n}}{[S_r^2]^n} = (2n-1)!!. \quad (4)$$

This ratio is independent of the scale  $r$ , and therefore, the intermittent exponent  $\zeta = 0$ . Thus, a Gaussian field is not intermittent. Moreover, not all non-Gaussian fields are intermittent. Only fields, for which the ratio in eq. (1) diverges as  $r \rightarrow 0$ , are intermittent.

For a lognormal field, the probability distribution function (PDF) of  $\Delta_r^2(x)$  is

$$P[\Delta_r^2(x)] = \frac{1}{2^{1/2}\pi^{1/2}\Delta_r^2(x)\sigma(r)} \exp\left\{-\frac{1}{2}\left(\frac{\ln\Delta_r^2(x) - \ln\Delta_r^2(x)_m}{\sigma(r)}\right)^2\right\}, \quad (5)$$

where  $\Delta_r^2(x)_m$  is the *median* of  $\Delta_r^2(x)$  (Vanmarcke 1983). The variance  $\sigma(r)$  of  $\ln\Delta_r^2(x)$  may be a function of the scale  $r$ . Using eq. (5), we have

$$\frac{S_r^{2n}}{[S_r^2]^n} = e^{(n^2-n)\sigma^2(r)/2}. \quad (6)$$

The intermittent exponent of a lognormal field is then

$$\zeta \simeq (n^2 - n)\sigma^2(r)/2\ln(r/L). \quad (7)$$

Because  $r < L$ ,  $\zeta$  is negative. Therefore, a lognormal field is intermittent.

In comparison with the Gaussian result (eq. (4)), the ratio of eq. (6) increases faster with  $n$ . This is due to the fact that a lognormal PDF is long-tailed. long-tailed PDF is a common property of intermittent fields. The property of  $S_r^{2n} \gg [S_r^2]^n$  on small scales indicates that the field contains ‘‘abnormal’’ events of large density fluctuations  $|\Delta_r(x)|$ . The events of big  $|\Delta_r(x)|$  correspond to a sharp increase or decrease of the field, and constitute the long-tail of the PDF of  $|\Delta_r(x)|$ .

### 3 DWT algorithm of power spectrum of Ly $\alpha$ transmitted flux

#### 3.1 The field of Ly $\alpha$ transmitted flux fluctuations

The transmitted flux of a QSO absorption spectrum is given by  $F(\lambda) = F_c(\lambda)e^{-\tau(\lambda)}$ , where  $F_c(\lambda)$  is the continuum,  $e^{-\tau(\lambda)}$  the transmission, and  $\tau(\lambda)$  the opacity. Since the observed data (§4) is already reduced by a continuum fitting, we have

$$F(\lambda) = e^{-\tau(\lambda)} + n(\lambda), \quad (8)$$

where the term  $n(\lambda)$  describes the stochastic noise including the Poisson noise of photon count. It satisfies the statistical properties

$$\langle n(\lambda) \rangle = 0, \quad \langle n(\lambda)n(\lambda') \rangle = \sigma^2(\lambda)\delta_{\lambda,\lambda'}^K, \quad (9)$$

where  $\delta^K$  is the Kronecker Delta function. The ensemble average is over the density fluctuations. Therefore, we have  $\langle F(\lambda) \rangle = \langle e^{-\tau(\lambda)} \rangle$ . Generally speaking,  $\langle F(\lambda) \rangle$  is still position-dependent, as it depends on the photoionization rate of HI, and the temperature of the IGM. Moreover, for a given scale  $r$ , all fluctuations on scales larger than  $r$  around the position  $\lambda$  act as a background for this fluctuation. This leads to a position dependent background. If one can assume that  $\langle F(\lambda) \rangle$  is a constant, then we have  $\langle F(\lambda) \rangle = \langle e^{-\tau(\lambda)} \rangle$ , which is the mean transmission.

The field of Ly $\alpha$  transmitted flux fluctuations are defined by

$$\delta^n(\lambda) = \frac{F(\lambda) - \langle F(\lambda) \rangle}{\langle F(\lambda) \rangle}, \quad (10)$$

or

$$\delta(\lambda) = F(\lambda) - \langle F(\lambda) \rangle. \quad (11)$$

$\delta^n(\lambda)$  and  $\delta(\lambda)$  are different by a normalisation factor  $\langle F(\lambda) \rangle$ . If  $\langle F(\lambda) \rangle$  is  $\lambda$ -independent, the unnormalised and normalised fields  $\delta^n(\lambda)$  and  $\delta(\lambda)$  differ only by a constant. If  $\langle F(\lambda) \rangle^2$  doesn't contain small scale fluctuations, then one still can treat  $\langle F(\lambda) \rangle^2$  as a constant when studying the fields on small scales.

### 3.2 DWT variables of Ly $\alpha$ transmitted flux field

In order to easily illustrate the effect of intermittency on the power spectrum, we calculate the power spectrum of Ly $\alpha$  transmitted flux with the discrete wavelet transform (DWT).

We use  $x_1$  and  $x_2$  to denote the spatial range of a flux field corresponding to the wavelength range from  $\lambda_1$  and  $\lambda_2$ . To implement a DWT scale-space decomposition of a flux field  $F(x)$ , we first chop the spatial range  $L = x_2 - x_1$  of the 1-D sample into  $2^j$  subintervals labelled with  $l = 0, \dots, 2^j - 1$ . Each subinterval spans a spatial range  $L/2^j$ . The subinterval  $l$  is from  $x_1 + Ll/2^j$  to  $x_1 + L(l+1)/2^j$ . The index  $j$  can be an integer. Thus, we decompose the space  $L$  into cells  $(j, l)$ , where  $j$  denotes the scale  $L/2^j$ , and  $l$  the spatial range  $[x_1 + Ll/2^j, x_1 + L(l+1)/2^j]$ .

Corresponding to each cell (or mode)  $(j, l)$ , there is a scaling function  $\phi_{jl}(x)$ , and a wavelet function  $\psi_{jl}(x)$ , which are the orthogonal and complete basis for the scale-space decomposition. The most important property of the DWT basis is its locality in both scale and physical (or redshift) spaces. The scaling function  $\phi_{jl}(x)$  is a window function on scale  $j$  and at the position  $l$ . The wavelet function  $\psi_{jl}(x)$  is admissible (Daubechies 1992), i.e.,  $\int \psi_{jl}(x) dx = 0$ . Therefore, it measures the fluctuation on scale  $j$  and at position  $l$ . All wavelets with compactly supported bases will produce similar results. We will use Daubechies 4 (D4) basis below, for its ease in numerical calculations among the compactly supported orthogonal bases. The D4 scaling function  $\phi_{jl}(x)$ , wavelet  $\psi_{jl}(x)$  and their Fourier transforms  $\hat{\phi}_{jl}(n)$ ,  $\hat{\psi}_{jl}(n)$  are shown in Yang et al (2001b).

Subjecting a transmitted flux  $F(x)$  to the DWT, we have (Daubechies 1992; Fang, & Thews 1998)

$$F(x) = \sum_{l=0}^{2^j-1} \epsilon_{jl}^F \phi_{jl}(x) + \sum_{j'=j}^{J-1} \sum_{l=0}^{2^{j'}-1} \tilde{\epsilon}_{j'l}^F \psi_{j'l}(x), \quad (12)$$

where  $J$  is given by the finest scale (pixel resolution) of the sample, i.e.,  $\Delta x = L/2^J$  and  $j$  is the scale we want to study. The field now is described by DWT variables  $\epsilon_{jl}^F$  and  $\tilde{\epsilon}_{jl}^F$ , which are called scaling function coefficient (SFC) and wavelet function coefficient (WFC), respectively.

The SFC is given by projecting  $F(x)$  onto  $\phi_{jl}(x)$

$$\epsilon_{jl}^F = \int F(x) \phi_{jl}(x) dx. \quad (13)$$

The SFC  $\epsilon_{jl}^F$  is proportional to the mean field at the mode  $(j, l)$ . The WFC is obtained by projecting  $F(x)$  onto  $\psi_{jl}(x)$

$$\tilde{\epsilon}_{jl}^F = \int F(x) \psi_{jl}(x) dx. \quad (14)$$

The WFC  $\tilde{\epsilon}_{jl}^F$  is basically the difference between  $F(x)$  and  $F(x+r)$ , where  $x \simeq x_1 + lL/2^j$  and  $r \simeq L/2^j$ . Thus, the WFC can be used to replace the variable  $F(x+r) - F(x)$ . Eq. (3) can then be rewritten as

$$S_j^{2n} = \langle |\tilde{\epsilon}_{jl}^F|^{2n} \rangle. \quad (15)$$

If the ‘‘fair sample hypothesis’’ (Peebles 1980) holds, one can replace the ensemble average in eq. (15) by a spatial average. We then have

$$S_j^{2n} = \frac{1}{2^j} \sum_{l=0}^{2^j-1} |\tilde{\epsilon}_{jl}^F|^{2n}. \quad (16)$$

### 3.3 Power spectra of Ly $\alpha$ transmitted flux

For a transmitted flux fluctuation field  $\delta^n(x)$ , the two point correlation function is defined by

$$\xi^n(\Delta x) = \langle \delta^n(x_1) \delta^n(x_2) \rangle, \quad (17)$$

where  $\Delta x = x_2 - x_1$ . Similarly, one can define a two point correlation function of the unnormalised field  $\delta(x)$  as

$$\xi(\Delta x) = \langle \delta(x_1) \delta(x_2) \rangle. \quad (18)$$

The Fourier counterparts of  $\xi^n(\Delta x)$  and  $\xi(\Delta x)$  are, respectively, the normalised and unnormalised power spectra,  $P^n(k)$  and  $P(k)$ .

The algorithm of the power spectrum for both  $P^n(k)$  or  $P(k)$  in the DWT representation has been developed (Pando & Fang 1998; Fang, & Feng 2000; Yang et al. 2001a, 2001b and Jamkhedkar, Bi, & Fang 2001). We will study only the unnormalised power spectrum  $P(k)$  below. If  $\langle F(\lambda) \rangle$  is constant, the normalised and unnormalised power spectra  $P^n(k)$  and  $P(k)$  differ only by a constant factor  $\langle F(\lambda) \rangle^2$ . In this case, all the results for  $P(k)$  also hold for  $P^n(k)$ . Problems with  $P^n(k)$  caused by a non-constant  $\langle F(\lambda) \rangle$  will be discussed in the conclusions.

The power spectrum in the DWT variables is given by

$$P_j = \frac{1}{2^j} \sum_{l=0}^{2^j-1} (\tilde{\epsilon}_{jl}^F)^2 - \frac{1}{2^j} \sum_{l=0}^{2^j-1} (\tilde{\epsilon}_{jl}^n)^2. \quad (19)$$

The first term on the r.h.s. of eq. (19) is the power of  $\delta(x)$  on scale  $j$ . The second term on the r.h.s. of eq. (19) is due to the noise given by

$$(\tilde{\epsilon}_{jl}^n)^2 = \int \sigma^2(x) \psi_{jl}^2(x) dx. \quad (20)$$

Comparing eq. (19) with eq. (16), we have  $P_j = S_j^2$ . Therefore, the power spectrum actually is the second moment of the PDF of  $\tilde{\epsilon}_{jl}^F$ .

It has been shown in general that the DWT power spectrum  $P_j$  of a random field  $\delta(x)$  is related to the Fourier power spectrum  $P(n)$  of the field as

$$P_j = \frac{1}{2^j} \sum_{n=-\infty}^{\infty} |\hat{\psi}(n/2^j)|^2 P(n), \quad (21)$$

where  $n$  is related to the wavenumber by  $k = 2\pi n/L$ . Therefore, the DWT power  $P_j$  is a banded Fourier power spectrum. Since for D4 wavelet  $|\hat{\psi}(\eta)|^2$  has peak at  $\eta \simeq 1$ , the band  $j$  is around the wavenumber  $k = 2\pi n/L \simeq 2\pi 2^j/L$ .

The difference between the DWT mode  $(j, l)$  and the Fourier mode  $k$  should be emphasised. For a given  $j$ , the size of a cell (mode) is  $L/2^j$ , which corresponds to wavenumber  $k = 2\pi 2^j/L$ . However, the wavelet function  $\psi_{jl}(x)$  is localised within  $L/2^j$ , and, therefore, the uncertainty relation  $\Delta x \Delta k = 2\pi$  gives  $\Delta k = 2\pi/(L/2^j) = k$ . That is, a DWT mode with  $j$  actually corresponds to a band of Fourier modes  $k \pm k/2$ , i.e., the relevant band is  $\Delta k/k = \Delta \ln k \simeq 1$ . This banding is optimised in the sense that to detect small scale fluctuations (larger wavenumber  $k$ ), the size of the pieces  $\Delta x$  is chosen to be smaller, while to detect large scale fluctuations (smaller wavenumber), the size of the pieces  $\Delta x$  is chosen to be larger. We sometimes characterise a DWT scale  $j$  by the Fourier mode  $k$ . In this case, the  $k$  is given by the maximum  $\eta_{max}$  of the Fourier transform  $|\hat{\psi}_{jl}(\eta)|$ .

## 4 Samples

### 4.1 Observed data

The observational data used in our study consists of 28 Keck HIRES QSO spectra (Kirkman, & Tytler 1997). The QSO emission redshifts cover a redshift range from 2.19 to 4.11. For each of the 28 QSOs, the data are given in form of pixels ( $i = 1, 2, \dots$ ) with wavelength  $\lambda_i$ , flux  $F(\lambda_i)$  and noise  $\sigma(\lambda_i)$ . The noise accounts for the Poisson fluctuations in the photon count, the noise due to the background and the instrumentation. The continuum of each spectrum is given by IRAF CONTINUUM fitting.

For our purpose, the useful wavelength region is from the Ly $\beta$  emission to the Ly $\alpha$  emission, excluding a region of about 0.06 in redshift close to the quasar to avoid any proximity effects. In this wavelength range, the number of pixels of the data is about  $1.2 \times 10^4$  for each spectrum. Fig. 1 shows the wavelength range for 30 QSOs. Since the data of Q0241-0146 has about 44% and, Q1330+0108 has about 27% pixels with S/N < 3, we will not use these QSOs in our analysis. We use only the 28 QSO forest samples.

For each bin in this data set, the ratio  $\Delta\lambda/\lambda$  is constant, i.e.,  $\Delta\lambda/\lambda \simeq 13.8 \times 10^{-6}$ , or  $\delta v \simeq 4.01$  km/s, and, therefore, the resolution is about 8 km/s. The distance between  $N$  pixels in the units of the local velocity scale is given by  $\Delta v = 2c(1 - \exp[-(1/2)N\delta v/c])$  km/s, or wavenumber  $k = 2\pi/\Delta v$  s/km. We use only  $2^{13} = 8192$  pixels of each spectrum. Thus, each cell on the DWT scale  $j$  corresponds to  $N = 2^{13-j}$  pixels.

This data set has been used for the Fourier power spectrum analysis (Croft et al 1999, 2002). They concluded that on scales  $k \leq 0.15$  s/km the contamination of noise is small. In order to easily compare our results with the Fourier analysis, we concentrate mainly on the DWT scales  $j \leq 10$ , or bin number  $N \geq 8$ ,  $k \leq 0.2$  s/km, or  $\Delta v \geq 32$  km/s.

The samples are contaminated by metal lines. It is generally believed that metal lines are narrow with a Doppler parameter  $b \leq 15$  km/s (Rauch, et al 1997; Hu et al 1995). We identified the big spikes on the scale  $\sim 32$  s/km for the ten QSOs (Q0014+8118, Q0054-2824, Q0636+6801, Q0642+4454, Q0940-1050, Q1017+1055, Q1103+6416, Q1422+2309, Q1425+6039, Q1759+7529) and checked if these are related to metal lines. To estimate the effect of metal lines, we compare the statistical results of metal-line-removed samples with those without removing metal lines.

In our analysis, we sometimes use the 28 QSO transmissions individually, i.e. calculate the statistics of the transmission over each QSO separately, and sometimes all the transmissions are treated together. In the latter case, we divide the data into 12 redshift ranges from  $z = 1.6 + n \times 0.20$  to  $1.6 + (n + 1) \times 0.20$  where  $n = 0, \dots, 11$ . All the transmission flux in a given redshift range forms an ensemble. Note that the number of data points in each redshift range is different.

The mean flux  $\langle F \rangle$  of these samples at  $z = 1.6$  is  $\sim 0.85$ , and decreases to  $\sim 0.5$  at  $z = 3.5$ . In each redshift range, the dispersions of  $\langle F \rangle$  are about 10-15%.

## 4.2 Treatment of unwanted data

Before calculating the DWT power spectrum of observed data, we discuss our method of treating unwanted data, including the pixels without data, contamination of metal lines, etc. On an average the S/N ratio of the Keck spectra is high. The mean  $1\sigma$  uncertainty in the flux values  $F$  relative to the continuum  $F_c$  in the Ly $\alpha$  forest region is 4% on an average (Croft et al 2002). However, for some pixels, the S/N is as low as about 1, such as pixels with negative flux. Most of these regions are saturated absorption regions. Although the percentage of pixels within these regions is not large, they may introduce large uncertainties in the analysis. We must reduce the uncertainty given by low S/N pixels.

The conventional technique of reducing these uncertainties is eliminating the unwanted bins and smoothly rejoining the rest of the forest spectra. However, by taking advantage of the localisation of wavelets we can use the algorithm of DWT denoising by thresholding (Donoho 1995) as follows

1. Calculate the SFCs of both transmission  $F(x)$  and noise  $\sigma(x)$ , i.e.

$$\varepsilon_{jl}^F = \int F(x)\phi_{jl}(x) dx, \quad \varepsilon_{jl}^N = \int \sigma(x)\phi_{jl}(x) dx. \quad (22)$$

2. Identify an unwanted mode  $(j, l)$  using the threshold condition

$$\left| \frac{\varepsilon_{jl}^F}{\varepsilon_{jl}^N} \right| < f, \quad (23)$$

where  $f$  is a constant. This condition flags all modes with S/N less than  $f$ . We can also flag modes dominated by metal lines.

3. Since all the statistical quantities in the DWT representation are based on an average over the modes  $(j, l)$ , we will skip all the flagged modes while computing these averages. Therefore no rejoining and smoothing of the data are needed.

We call this algorithm the conditional-counting method. It should be pointed out that condition eq. (23) is applied on each scale  $j$ , and therefore the unwanted modes are flagged on a scale-by-scale basis. If the

size of an unwanted data segment is  $d$ , condition eq. (23) only flags modes  $(j, l)$  on scales less than or comparable to  $d$ . We also flag two modes around each unwanted mode to reduce any boundary effects of the unwanted chunks.

Since the DWT calculation assumes that the sample is periodized, this may cause uncertainty at the boundary of the sample. To reduce this effect, we drop five modes neighbouring the boundary of the sample. With this method, we can still calculate the power spectrum by the estimators of eq. (19), but the average is not over all modes  $l$ , but over the un-flagged modes only.

### 4.3 Testing the DWT denoising method

At the first glance, the conditional-counting condition eq. (23) seems to preferentially drop modes in the low transmission regions, and may lead to an  $f$ -dependence of power spectrum. To test this problem, we calculate the power spectrum  $P_j$  of Q1700+6419. The conditional-counting parameter  $f$  is taken to be  $f = 1, 2, 3$  and 5. The results of  $P_j$  vs  $j$  are shown in Fig. 2.

Fig. 2 shows that the power spectrum  $P_j$  is independent of the parameter  $f$ . For other samples, the results are also the same. The reason can be seen from eq. (19), which shows that the contribution to the power  $P_j$  given by mode  $(j, l)$  is  $(\tilde{\epsilon}_{jl}^F)^2 - (\tilde{\epsilon}_{jl}^n)^2$ . The noise subtraction term  $(\tilde{\epsilon}_{jl}^n)^2$  guarantees that the contribution of modes with small  $S/N$  to  $P_j$  is always small. For instance, the modes with negative flux, i.e., the modes with flux having the same order of magnitude as noise, the two terms  $(\tilde{\epsilon}_{jl}^F)^2$  and  $(\tilde{\epsilon}_{jl}^n)^2$  cancel each other statistically. Thus, in the range of  $f \leq 5$ , all the flagged modes always have very small or negligible contributions to  $P_j$ . Denoising by thresholding is reliable. The thresholding method checks variables mode by mode, and therefore, can only be effectively applied for a space-scale decomposed field.

## 5 Intermittent features of local power

### 5.1 Spikiness of the spatial distribution of local power

Eq. (19) can be rewritten as

$$P_j = \frac{1}{N_f} \sum_{l=0}^{N_f} P_{jl}, \quad (24)$$

and

$$P_{jl} = (\tilde{\epsilon}_{jl}^F)^2 - (\tilde{\epsilon}_{jl}^n)^2, \quad (25)$$

where  $N_f$  is the number of modes remaining after applying the denoising condition of eq. (23). Eq. (24) shows that the power spectrum  $P_j$  is the average of local power  $P_{jl}$ . For a given  $l$ , the  $j$ -distribution of  $P_{jl}$  is the local power spectrum, i.e., the power spectra in the spatial range of  $l$ . For a given  $j$ , the  $l$ -distribution of  $P_{jl}$  is the spatial distribution of local power.

The spatial distribution of local powers is very intuitive for the demonstration of intermittency. Fig. 3 shows a typical spatial distribution of the local power of the transmitted flux. The left panels of Fig. 3 are  $P_{jl}/P_j$  for  $j = 9$  and 10 ( $\sim 64$  km/s and 32 km/s, respectively). The right panels represent the corresponding distribution of the phase-randomised (PR) data. The PR data are obtained by taking the inverse transform of the Fourier coefficients of the original data after randomising their phases uniformly over  $[0, 2\pi]$  without changing the amplitudes. This gives rise to a PR field with the same unnormalised power spectrum as the original field. The mean unnormalised powers of the left and the right panels of Fig. 3 are actually the same. Note that, in Fig. 3 large spikes corresponding to metal lines have been removed.

Two main features can be observed in Fig. 3. First, the local power distributions of  $P_{jl}/P_j$  on  $j = 9$  and 10 (left panels) are significantly different from their counterparts of the PR sample (right panels). The former show spiky structures, while the latter are noisy distributions. Therefore, the spikiness arises completely from the phase correlation of the Fourier modes. Second, the spiky structures are more significant on smaller scales, or larger  $j$ . That is, the ratio between the amplitudes of the spikes and the mean power is higher on smaller scales.

Although spikes correspond to a large difference in the flux  $|F(x + \Delta x) - F(x)|$ , they are not always related to Ly $\alpha$  absorption lines or sharp edges of saturated regions. This is because the strength of spikes is

measured by the ratio  $P_{jl}/P_j$ . Fig. 2 shows that the mean power of transmission flux fluctuations on  $j = 10$  is about  $P_{10} \leq 10^{-2}$ . Thus, even for a spike as high as  $P_{jl}/P_j \sim 40$  at  $j = 10$ , the flux difference is only  $|F(x+L/2^{10}) - F(x)| \simeq 0.6$ , which is less than  $\langle F \rangle = 0.7$  and does not require either  $F(x+L/2^{10})$  or  $F(x)$  to equal zero. Therefore, spikes are different from the Ly $\alpha$  absorption lines which correspond to valleys identified by a Voigt profile fitting.

The difference between the spikes and Ly $\alpha$  absorption lines can also be seen from Fig. 4, which shows the local power  $P_{jl}$  on scale  $j = 10$  against the corresponding  $\sqrt{2^j/L}\mathcal{E}_{jl}^F$  on scales  $j = 10$  and  $j = 11$  at the same physical position  $l$ . Since  $\sqrt{2^j/L}\mathcal{E}_{jl}^F$  is the flux smoothed on scale  $j$ , absorption lines having a width of the order of  $j$  corresponds to  $\sqrt{2^j/L}\mathcal{E}_{jl}^F \simeq 0$ . Fig. 4 shows the modes with top 1 % power among all modes of the 28 QSOs combined. All these local powers  $P_{jl}$  are larger than  $10P_j$ , and therefore, they are spikes. One can see from Fig. 4 that most spikes are not related to saturated regions with  $F \sim 0$  or  $\sqrt{2^j/L}\mathcal{E}_{jl}^F \sim 0$ .

## 5.2 PDF of local powers

By definition, spikes correspond to structures of large  $|F(x + \Delta x) - F(x)|$ . A spiky field indicates the excess of large transmission fluctuations compared to a Gaussian distribution. Thus, the non-Gaussianity of a spiky field can be described by the PDF or the one-point distribution of local power  $P_{jl}$ .

To calculate the PDF, we use the 12 redshift ranges of the samples mentioned in §4.1. For each redshift range, we construct an ensemble consisting of all  $P_{jl}$  from the 28 QSOs, for which the position  $l$  is in the redshift ranges. Fig. 5 plots the PDFs of  $P_{jl}/P_j$  on the scale  $j = 10$  in the 12 redshift ranges.

If the field  $\delta(x)$  is Gaussian, the PDF of  $\tilde{\mathcal{E}}_{jl}^F$  is also Gaussian. Thus, the PDF of  $y = P_{jl}/P_j$  should be a  $\chi^2(N = 1)(y)$  distribution, which is also plotted in Fig. 5 (solid line). Comparing to the  $\chi^2(N = 1)$ -distribution, the PDFs of the Keck data are generally higher at  $P_{jl}/P_j \sim 0$ , lower at  $P_{jl}/P_j \sim 1$ , and again higher at  $P_{jl}/P_j \geq 10$ . That is, for most modes the local powers are low or close to zero, while rare modes have high power (long-tail).

In Fig. 5, five of the 12 PDFs have tails as long as  $P_{jl}/P_j > 32$ , and six have  $P_{jl}/P_j > 10$ . The number of long-tails cannot directly be used to measure the degree of the spikiness, as different PDFs of Fig. 5 are given by different number of independent modes. Nevertheless, it is clear that all the long-tail events have a much larger probability than a Gaussian.

Fig. 6 shows the PDF of the local power  $P_{jl}/P_j$  in the redshift range  $2.8 \leq z \leq 3.0$  on scales  $j = 8, 9$  and  $10$ , with the parameter in eq. (23),  $f = 1$  (top),  $f = 3$  (middle) and  $f = 5$  (bottom). We see from Fig. 6 that the observed PDF is independent of the parameter  $f$ . The observed PDF of  $P_{jl}/P_j$  at  $j = 8$  is consistent with the  $\chi^2$  distributions, but it is long-tailed for  $j = 9$  and  $10$ . At  $j = 10$ , the long-tail is given by  $P_{jl}/P_j \simeq 32$ . A spike with  $P_{jl} > 32P_j$  corresponds to an event  $\sim 5.6\sigma$ . In Fig. 6, we use 2100  $P_{jl}/P_j$  data points (modes) for the statistics on  $j = 10$  and  $f = 3$ , and therefore the observed probability of the  $5.6\sigma$  event is about  $4 \times 10^{-4}$ . This is much larger than the Gaussian probability of an  $5.6\sigma$  event.

In contrast to Figs. 5 and 6, Fig. 7 shows the PDF of  $P_{jl}/P_j$  for a PR sample. As expected the PR field follows the  $\chi^2(N = 1)$ -distribution on small scales ( $j = 10$ ).

Some errors in Figs. 5 and 6 might be caused by the 10% dispersion of the mean flux (§4.1). As each ensemble in a given redshift range contains local power modes  $P_{jl}$  from different QSOs, which have different mean flux  $\langle F(x) \rangle$ . However, this error will not change the intermittent features. This can be seen from Fig. 8, which gives the PDF of  $P_{jl}/P_j$  for *one* sample Q0014+8118 at  $j = 10$ . Fig. 8 actually shows exactly the same features as in Figs. 5 and 6.

Moreover, Fig. 8 gives the distribution  $P_{jl}/P_j$  for the sample Q0014+8118 with and without removing high spikes located in the regions contaminated by metal lines. The figure shows the existence of a long-tail regardless of whether the metal lines and metal line suspects are removed or not. Other quasars searched for metal lines show similar results.

Therefore, the long-tail seems to be a permanent feature of the PDF of local power. It is not caused by noise or other contamination. To measure the long-tail we add a lognormal PDF in Fig. 8 given by

$$P(y) = \frac{1}{2^{1/2}\pi^{1/2}y\mu} \exp \left\{ -\frac{1}{2} \left( \frac{\ln y + \mu^2/2}{\mu} \right)^2 \right\}. \quad (26)$$



For this PDF, the mean of  $y$  is always equal to 1, i.e.,  $\bar{y} = 1$ . The parameter  $\mu$  measures the long tail. Larger the  $\mu$ , longer the tail. The best fitting to the observed long-tail is  $\mu \simeq 1.5$ . The observed long-tail is longer than lognormal PDFs. The PDF of the flux field  $\delta(x)$  has a more prominent long-tail than a lognormal field.

## 6 Intermittency and the precision of power spectrum

### 6.1 Domination of power spectrum by spikes

As shown by eq. (24), the power spectra,  $P_j$ , are given by the mean of local powers over independent modes  $l = 1, \dots, N_f$ . When the spiky features are pronounced, the power of the transmission fluctuations is concentrated in the spikes, and therefore, a big fraction of the power in eq. (24) actually is dominated by the spikes.

To demonstrate the spikiness, we calculate the power spectrum by averaging local power  $P_{jl}$  in the 12 redshift ranges. We also calculate the averages over 12 local power ensembles, but dropping the top 1%, 3% and 5% of the local power modes. We plot the ratio of power after dropping the highest modes to the power without dropping any modes. The result is shown in Fig. 9.

One can see from Fig. 9 that for most cases, dropping the top 5% modes leads to a decrease in  $P_j$  by a factor equal to or larger than 2. That is, 50% or even more of the power is given by the top 5% modes. On scale  $j = 10$ , dropping the top 1% modes leads to a 20% or more decrease in  $P_j$ . If the field were Gaussian, a top 1% elimination of data would lead to a decrease in  $P_j$  of no more than 3%, and a top 5% elimination would lead to a decrease of no more than 8%. Therefore, Fig. 9 shows that the power spectrum is substantially dependent on the rare events – high spikes. The power is concentrated in the spikes. As a consequence, the number of effective modes of the random field is significantly reduced, i.e., only the rare modes contribute to the measurement of the power spectrum, while other modes are inactive. This will lead to uncertainty in the power spectrum.

### 6.2 Uncertainty in the power spectrum of an intermittent field

Generally, the uncertainty in the power spectrum can be effectively reduced by increasing the number of independent modes of measurement. Using the “fair sample hypothesis” (Peebles 1980), we first construct an ensemble of samples by dividing the observed sample into a set of  $N$  subsamples. We then calculate the mean and variance over the ensemble. The precision of the power measurement would then be improved if the number  $N$  is large, as the error is  $\propto \sqrt{1/N}$ . If this is always true, then we should divide the sample into as many independent subsamples as possible.

To detect the power of Ly $\alpha$  transmitted flux fluctuations on the scale  $k$ , the largest possible number  $N$  is given by the uncertainty relation  $\Delta x \Delta k \simeq 2\pi$ . Therefore, we should divide the 1-D flux field  $(x_1, x_2)$  into segments with size  $\Delta x \geq 2\pi/k$ . In this case,  $\Delta k \leq k$ . The segment gives valuable information of the power in the band  $k \pm \Delta k$ . This is just what the DWT does. The local power  $P_{jl}$ , given by DWT, provides the largest possible number of modes for detecting power in the band corresponding to  $k$ .

However the precision improvement factor  $\sqrt{1/N}$  is largely based on the central limit theorem. Let us consider eq. (24) to be a definition of the stochastic variables  $P_j$  constructed from the stochastic variables  $P_{jl}$ . According to the central limit theorem if all  $P_{jl}$  are independent variables, having identical PDFs, then  $P_j$  will approach a Gaussian PDF when  $N_f$  is large, regardless of the PDF of  $P_{jl}$ . Actually, the convergence of  $P_j$  to a Gaussian variable is fast as  $N_f$  increases. This result ensures that the error of power spectrum  $P_j$  is basically proportional to the Gaussian factor  $\sqrt{1/N_f}$ , even when the field is nonlinear and non-Gaussian.

Yet, the central limit theorem does not work well with fields having a divergent ratio between its moments [eqs.(1) or (2)]. Principally, a superposition of intermittent fields will also converge to a Gaussian limit. The error will decrease as  $\sqrt{1/N_f}$  as required by the central limit theorem. However, this needs a large number  $N_f$ . This is because the central limit theorem relies on the existence of a unique relationship between the PDF and moments (Vanmarcke 1983). The PDF of a lognormal field is not uniquely determined by its moments (Crow, & Shimizu 1988). This leads to a very slow convergence of the PDF of  $P_j$  to the limiting Gaussian PDF as  $N_f$  increases. The PDF of  $P_j$  is still long tailed if the PDF of  $P_{jl}$  is long-tailed, like a lognormal field. The number  $N_f$  needed for the convergence to a Gaussian  $P_j$  can be estimated by

Table 1

$N_f$	$P_j$	$\sigma_P$	95% confidence	99% confidence
99	0.134	0.215 (0.250)	< 0.844 (0.823)	< 0.999(1.85)
198	0.132	0.231 (0.246)	< 0.835 (0.810)	< 1.30 (1.82)
397	0.120	0.224 (0.223)	< 0.827 (0.736)	< 1.30 (1.65)

(Barakat, 1976) as,

$$N_f \simeq \gamma_1^2, \quad (27)$$

where  $\gamma_1 = (e^\mu - 1)^{1/2}(e^\mu + 2)$  is the skewness of the PDF eq. (26). Thus, for  $\mu \simeq 1.5$  (§5.2), we have  $N_f \simeq 2.1 \times 10^4$ . Therefore, the central limit theorem is less effective for an intermittent field. For the PDF shown in Fig. 8, the precision improvement factor  $\sqrt{1/N}$  would not work until  $N_f$  is not large enough as required by eq. (27).

To demonstrate this property, we calculate the mean power and its 1- $\sigma$  of Q0014+8118 on the scale  $j = 9$ . The power is calculated by eq. (24), and the 1- $\sigma$  by

$$\sigma_P = \left[ \frac{1}{N_f - 1} \sum_{N_f} (P_{jl} - P_j)^2 \right]^{1/2} \quad (28)$$

In the redshift range 2.7 - 3.12, there are 397 local power modes  $P_{jl}$  available. These powers are independent in the sense that the cross correlations  $\langle \tilde{\epsilon}_{jl}^F \tilde{\epsilon}_{j'l'}^F \rangle \simeq 0$  if  $l \neq l'$  (Pando, Feng, & Fang 2001). However, the PDF of these  $P_{jl}$  are close to eq. (26). The results are given in Table 1. Here  $N_f$  means that we use only the first  $N_f$  local power modes  $P_{jl}$  out of the total 397 modes. Table 1 shows that  $\sigma_P$  does not show the  $\sqrt{1/N_f}$ -dependence. It is almost independent of  $N_f$ . On the other hand, we find the PR samples do show a decrease in the error by factor  $1/\sqrt{N_f}$ .

The numbers in the bracket of Table 1 are calculated by using the PDF in eq. (26), which gives

$$\sigma_P = P_j(e^\mu - 1)^{1/2}, \quad 95\% \text{ Con.} = P_j e^{1.96\mu - \mu^2/2}, \quad 99\% \text{ Con.} = P_j e^{2.58\mu - \mu^2/2}. \quad (29)$$

We use  $\mu = 1.5$ . All the observed results can roughly be fitted by the lognormal PDF eq. (26). That is, regardless of  $N_f$  in the range 99 - 397, the PDF of  $P_j$  are long-tailed. Again, with the phase randomised samples, the PDF of  $P_j$  is Gaussian, and with a variance following the factor  $1/\sqrt{N_f}$ .

Therefore, the variance  $\sigma_P$  doesn't effectively decrease with the increase of the number  $N_f$  when  $N_f$  is the order of  $\simeq 10^2$ . Table 1 shows also that the values of  $\sigma_P$  generally are large. This is directly due to the intermittency, or the PDF eq. (26).

### 6.3 Error estimation by subsamples with optimal size

To reduce the uncertainty or 1- $\sigma$  error of the power spectrum of the flux fields, a popular method for estimating the error of power spectrum of the flux field is based on subsamples or segments with optimally selected size. For instance, Croft et al. (2002) used the jackknife error estimator, which is found by dividing the sample into  $N$  subsamples, and computing the 1- $\sigma$  error bars by  $\sigma_P = [(1/N) \sum_N (P_i - \hat{P})^2]^{1/2}$ , where  $\hat{P}$  is the mean power from the full data samples and  $P_i$  is the mean power estimated by leaving out the subsample  $i$ . They used  $N = 5$  as the optimal number. McDonald et al. (2000) used a modified bootstrap error estimator, in which they have re-sampled the data not pixel-by-pixel, but segment-by-segment. Each segment has a size of 100 pixels which is also used as an optimal number.

The 1- $\sigma$  error given by these methods is indeed much less than the  $\sigma_P$  listed in Table 1. We need to understand why they yield smaller error bars? What is the criterion for selecting the optimal size of subsamples and segments? In our view, these problems are not all technical, but rather depend on the intermittent nature of the Ly $\alpha$  flux field.

Table 2

	$N$	$M_i$	$P_j$	$\sigma_P$	95% Con.	99% Con.
1	397	1	0.120	0.224	< 0.827	< 1.30
2	40	9	0.123	0.073	< 0.233	< 0.282
3	20	19	0.121	0.044	< 0.208	< 0.215
4	10	39	0.121	0.015	-	< 0.143
5	5	79	0.120	0.015	-	< 0.143

To demonstrate these problems, we analyse the local power  $P_{jl}$  modes. The jackknife estimator is equivalent to dividing a total of  $N_f$  local power modes ( $P_{jl}$ ) into  $N$  groups (subsamples). Each group contains  $M$  modes, i.e.,  $N_f = NM$ . The  $1 - \sigma$  uncertainty is calculated by

$$\sigma_P = \left[ \frac{1}{N-1} \sum_{i=1}^N (P_i - P_j)^2 \right]^{1/2}, \quad (30)$$

and

$$P_i = \frac{1}{M_i} \sum_{l(i)} P_{jl}^i, \quad (31)$$

where the subscript and superscript  $i$  is for the group (subsample)  $i$ ,  $i = 1, \dots, N$ . The summation runs over modes  $l$  in the group  $i$ .

Using eqs. (30) and (31), we again calculate the mean and  $\sigma_P$  of the  $j = 9$  power of Q0014+8118. The result is listed in Table 2. Line 1 of Table 2 is the same as that of Table 1. It is for  $N = 397$ , and  $M_i = 1$ . The lines 2 through 5 are obtained by dividing the 397 local power modes ( $P_{jl}$ ) into 40, 20, 10 and 5 subsamples, respectively. When the size of subsamples is 9 and 19 (lines 2 and 3),  $\sigma_P$  is still large, and the numbers for 95% Con. and 99% Con. are also larger than  $2\sigma_P$  and  $2.5\sigma_P$ . Therefore, the PDF of  $P_i$  is still long-tailed. In the lines 4 and 5, we didn't show the 95% Con. level, because the total number  $N$  of the subsamples is only 10 or 5, and is too small to measure the PDF with a resolution  $< 10\%$ . The value of 99% Con. indicates that the PDF of  $P_i$  in the lines 4 and 5 probably is no longer long-tailed. The value of  $\sigma_P$  for lines 4 and 5 is much less than lines 1 and 2. Thus, with Table 2, the optimal size of the subsamples probably seems to be  $M \sim 40$  or  $80$  or  $N = 10$  or  $5$ . We also calculated powers on other scales and found that they have the similar behaviour as the Table 2. Therefore, the criterion for the optimal size  $M$  might be that the PDF of  $P_j$  is no longer long-tailed.

From Table 2, we see that the error estimator of subsamples or segments with optimal size calculates the dispersion of powers among the subsamples and segments only, and therefore, it actually is not a measure of the dispersion among all independent modes of the data. If two subsamples have the same mean power  $P_i$ , but very different distributions of  $P_{jl}$ , their contribution to  $\sigma_P$  (eq. (30)) is the same. Therefore,  $\sigma_P$  does not measure the uncertainty caused by the difference between the intermittent subsamples. Only when the two subsamples are Gaussian, their statistical properties would be the same if they have the same  $P_j$  (second moment). Therefore, the error estimator with subsamples and segments implicitly *assumes* that the subsamples are Gaussian. Eq. (30) with the optimal size subsamples does not give the error of the originally intermittent field, but the corresponding Gaussian subsamples having the same  $P_i$  as the intermittent field. We have checked the PDF of  $P_{jl}$  of subsamples in lines 4 and 5 of Table 2. There are substantially non-Gaussian.

Therefore, the improvement in the error estimation using optimal size subsamples or segments essentially is to replace an intermittent field within each subsamples with a Gaussian field. The intermittent features of the field are overlooked. Moreover, these errors are parameter (optimal size) dependent. According to eq. (1), the spikiness is scale-dependent, and therefore, the optimal size given by Table 2 generally is scale-dependent. One parameter option cannot fit the optimal size for all scales.

Table 3

$N_f$	$N_B$	$P_j$	$\sigma_P$	95% Con.	99% Con.
397	397	0.120	0.0110	< 0.140	< 0.153
198	198	0.119	0.0159	< 0.145	< 0.162
99	99	0.120	0.0231	< 0.167	< 0.185

## 6.4 Error estimation without subsamples

The analysis of last subsection shows that it is necessary to have an error estimator for the Ly $\alpha$  flux field, that does not require any extra parameters like the size of subsamples, and is not insensitive to the intermittency of the field. This can be done with the local power  $P_{jl}$ . Let us consider eqs. (24) and (28) once again. As mentioned in §6.2, the  $N_f$  data of  $P_{jl}$  can be considered independent. They can be used as the parent sample for bootstrap resampling. That is, we generate  $N_f$  samples having  $N_f$  modes by drawing  $P_{jl}$  from the parent sample with replacement. We then calculate the mean and 1- $\sigma$  over  $N_f$  realizations.

With this method, we again calculate the mean and  $\sigma_P$  on  $j = 9$  for Q0014+8118. First, Fig. 10 plots the PDF of the parent data of  $P_{jl}$  ( $j = 10$ ) of Q1103, and two given by bootstrap realizations. It shows that the PDF of the synthetic data  $P_{jl}^S$  of each realization is the same as the original  $P_{jl}$ , i.e., it is long-tailed. Therefore, the ensemble of the realizations from the bootstrap resampling contains all information of the intermittency.

The results of the mean and  $\sigma_P$  are listed in Table 3. Here  $N_B$  is the number of samples given by bootstrap re-sampling. We see, all the results are very stable. Except for  $N_f = 99$ , the relations among  $\sigma_P$ , 95% Con. and 99% Con. for  $N_f = 397$  and 198 are close to Gaussian. This is because the total number of modes used in the estimation of Table 3 is of the order of  $> 10^2 \times 10^2 \simeq 10^4$ , which is comparable with the number required by the central limit theorem (§6.2). The case of  $N_f = 99$  is not large enough, and gives a much larger  $\sigma_P$ . Therefore, this method illustrates a slow convergence of  $P_j$  to the Gaussian limit due to intermittency.

As a final result, we show in Fig. 11 the mean power  $P_j$  and their error bars on scales  $j = 8, 9$  and 10 given by the estimator of the bootstrap resampling developed above. The powers in Fig. 11 are shown in each redshift bin of the Keck data. As the field is highly non-Gaussian, we use confidence level to describe the uncertainty range. The error bars are the 99% confidence range of the bootstrap resampling. The error bars are independent of the parameter  $f$ , which is taken to be 1 (circle), 3 (triangle) and 5 (pentagon).

Fig. 11 shows clearly the effect of intermittency. The error bars at  $z \simeq 1.7$  and 1.9 are much larger than others, because these samples are not large enough. For redshift bins, for which the number of independent modes matches the condition of the CLT convergence, this bootstrap resampling method effectively reduces the uncertainty in the power spectrum without introducing extra parameters.

## 7 Discussion and conclusions

The most popular statistical measure in large scale structure study is the power spectrum. For Gaussian fields, there are many effective and successful algorithms of calculating the power spectrum and estimating their errors. The power spectrum in the nonlinear regime is also important not only for constraining cosmological parameters, but determining the initial conditions for the simulations of galaxy formation. However, the effects of non-Gaussianity upon the power spectrum have not been fully studied yet.

We studied the effect of the non-Gaussianity of the field of QSO Ly $\alpha$  transmitted flux fluctuations on the estimation of their power spectrum and errors. The flux field is intermittent. Generally speaking, intermittency poses problems in the detection of power spectrum, as a large fraction of the power of the transmission fluctuations is concentrated in rare and improbable events: high spikes. Thus, the power spectrum is sensitive to small probability events. Therefore, the dispersion among the different spatial regions is large. This property directly challenges the application of the ‘‘fair sample hypothesis’’ (Peebles 1980) which assumes that a part of the universe is a fair sample of the whole and ensemble averages can be calculated by spatial averages. That is, the spatial average will not converge to the ensemble averages

if the dispersion among the different spatial regions is large. Mathematically, this is shown by the slow convergence of  $P_j$  to the Gaussian limit required by the central limit theorem, if the PDF of the field is long-tailed due to intermittency.

To reasonably estimate the uncertainty of the power spectrum, we should carefully analyse the convergence of the data set considered, to the CLT. With this result, we show that some conventional methods essentially estimate the errors by the dispersion of the powers among subsamples, ignoring the dispersion among all the independent modes of the data. They do not measure the error of the non-Gaussian or intermittent field, but a Gaussian field. The error given by this method is parameter-dependent.

With analysis of the CLT convergence, we proposed an error estimator for the power spectrum. It is based on a bootstrap resampling among the local powers of all the modes. This estimation doesn't need any extra parameter like the size of subsamples, and doesn't ignore the intermittency of the fields. The powers and errors for 28 transmitted flux samples are calculated with this method. This result shows the effect of intermittency on power spectrum, and gives a more effective estimation of errors than the "optimal" size method, especially when the number of independent modes matches the condition of the CLT convergence.

We studied in this paper only the unnormalised power spectrum eq. (18), but not the normalised power spectrum eq. (17). If the normalisation is given by a constant  $\langle F(\lambda) \rangle^2$ , all the results for unnormalised power spectrum hold for the normalised power spectrum. If the background  $\langle F(\lambda) \rangle^2$  is not constant but position dependent, the local fluctuations will couple with the background when the field is non-Gaussian (Jamkhedkar, Bi, & Fang, 2001). This case should be studied in detail for the detection and error estimation of the normalised power spectrum.

## Acknowledgements

We thank J. Pando and H. G. Bi for their comments. LLF acknowledges support from the National Science Foundation of China (NSFC) and National Key Basic Research Science Foundation. PJ was supported by the Deans Dissertation Fellowship from the University of Arizona. PJ would also like to thank Drs. Stein and Shupe and the Department of Physics at the University of Arizona for their support.

## References

- [1] Baraket R., 1976, J. Opt. Soc. Am., 66, 211
- [2] Bi H. G., 1993, ApJ, 405, 479
- [3] Bi H. G., & Davidsen A. F., 1997, ApJ, 479, 523
- [4] Bi H. G., Ge J., & Fang L. Z., 1995, ApJ, 452, 90
- [5] Croft R. A. C., Weinberg D. H., Pettini M., Hernquist L., & Katz N., 1999, ApJ, 520, 1
- [6] Croft R., Weinberg D., Bolte M., Burles S., Hernquist L., Katz N., Kirkman D., Tytler D., 2002 astro-ph/0012324
- [7] Crow E. L., & Shimizu K., 1988, *Lognormal Distribution* (Marcel Dekker, New York)
- [8] Daubechies I., 1992, *Ten Lectures on Wavelets* (SIAM, Philadelphia PA)
- [9] Donoho D. L., 1995, IEEE Trans. Inf. Theory, 41, 613
- [10] Fang L. Z., Bi H. G., Xiang S. P., & Börner G., 1993, ApJ, 413, 477
- [11] Fang L. Z., & Feng L. L., 2000, ApJ, 539, 5
- [12] Fang L. Z., & Thews R., 1998, *Wavelets in Physics* (World Scientific, Singapore)
- [13] Farge M., Kevlahan N., Perrier V., & Goirand E. 1996, Proceedings of the IEEE, 84, 639

- [14] Feng L. L., & Fang L. Z., 2000, ApJ, 535, 519
- [15] Feng L. L., & Fang L. Z., 2001, ApJ, 554, 841
- [16] Feng L. L., Pando J., & Fang L. Z., 2001, ApJ, 555, 74
- [17] Gärtner J., & Molchanov S.A., 1990, Commun. Math. Phys., 132, 613
- [18] Hu E., Kim T.-S., Cowie L. L., Songaila A., & Rauch M., 1995, AJ, 110, 1526
- [19] Hui, L., & Gnedin N. Y., 1997, MNRAS, 292, 27
- [20] Jamkhedkar P., Zhan H., & Fang L. Z., 2000, ApJ, 543, L1
- [21] Jamkhedkar P., Bi H. G., & Fang L. Z., 2001, ApJ, 561, 94
- [22] Jamkhedkar P., 2002, *Intermittency in Large Scale Structures in the Universe*, Ph.D. thesis, University of Arizona, Tucson (<http://www.ece.umd.edu/~priyaj>)
- [23] Jones B. T., 1999, MNRAS, 307, 376
- [24] Kirkman D., & Tytler D., 1997, ApJ, 484, 672
- [25] Matarrese S., & Mohayaee R., 2002, MNRAS, 329, 37
- [26] McDonald P., Miralda-Escud'e J., Rauch M., Sargent W. L. W., Barlow T. A., Cen R., & Ostriker J. P., 2000, ApJ, 543, 1
- [27] Nusser A., & Haehnelt M., 1999, MNRAS, 303, 179
- [28] Pando J., & Fang L. Z., 1998, Phys. Rev. E57, 3593
- [29] Pando J., Feng L. L., & Fang L. Z., 2001, ApJ, 554, 841.
- [30] Pando J., Feng L. L., Jamkhedkar P., Zheng W., Kirkman D., Tytler D., & Fang L. Z., 2002, ApJ, 574, 575
- [31] Peebles P. J. E., 1980, *The large scale structure of the universe* (Princeton University Press, Princeton NJ)
- [32] Rauch M., Miralda-Escud'e J., Sargent W., Barlow T., Weinberg D., Hernquist L., Katz N., Cen R., Ostriker J., 1997, ApJ, 489, 7
- [33] Vanmarcke E., 1983, *Random Fields* (MIT Press, Cambridge MA); Web edition, 1998, by Rare Book Services, Princeton University (Princeton NJ) <http://www.princeton.edu/~evm/randomfields.html>
- [34] Yang X. H., Feng L. L., Chu Y. Q., & Fang L. Z., 2001a, ApJ, 553, 1
- [35] Yang X. H., Feng L. L., Chu Y. Q., & Fang L. Z., 2001b, ApJ, 560, 549
- [36] Yang X. H., Feng L. L., Chu Y. Q., & Fang L. Z., 2002, ApJ, in press, astro-ph/0110530
- [37] Zel'dovich Ya. B., Ruzmaikin A. A., & Sokoloff, D.D., 1990, *The Almighty Chance* (World Scientific, Singapore)
- [38] Zhan H., Jamkhedkar P., & Fang L. Z., 2001, ApJ, 555, 58
- [39] Zhan H., & Fang L. Z., 2002, ApJ, 566, 9

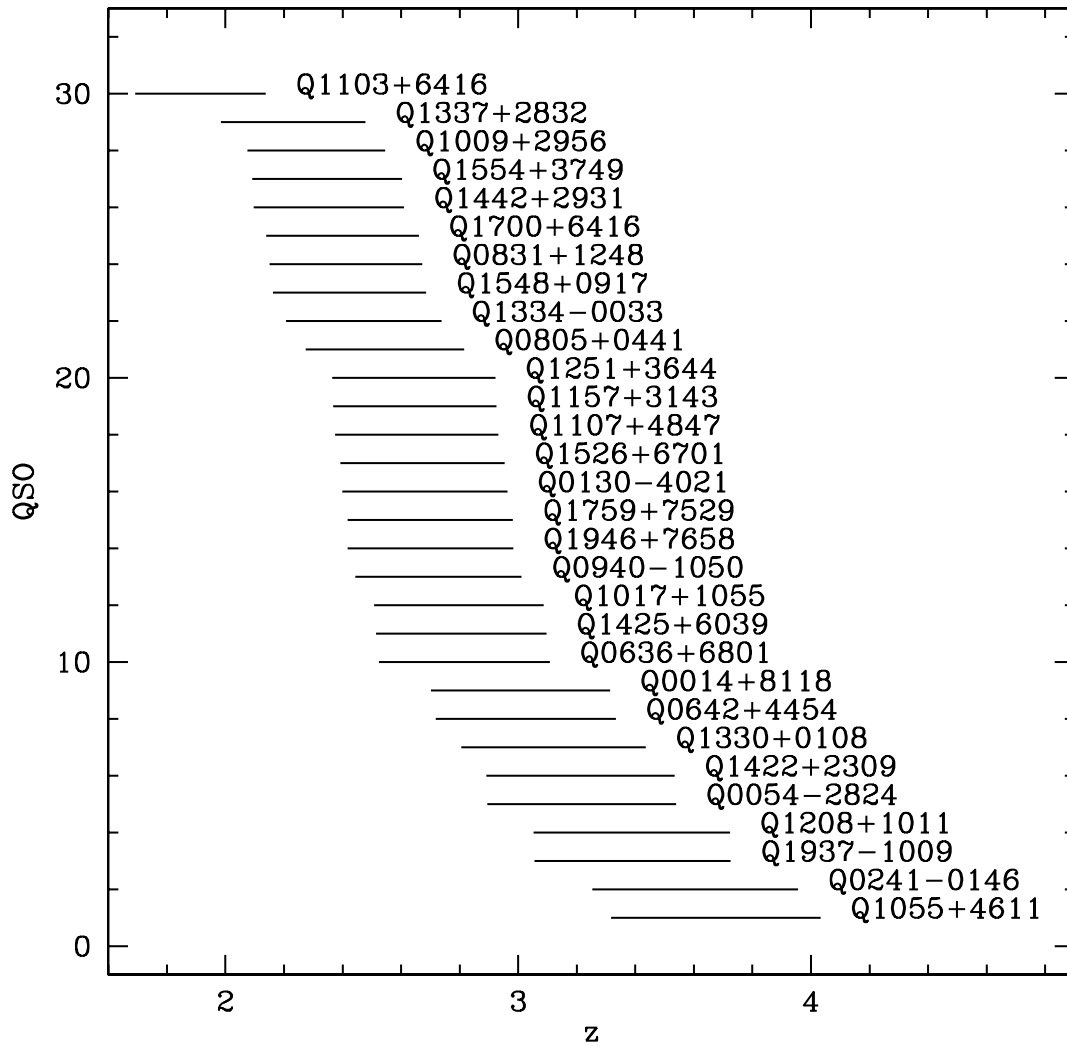


Figure 1: Redshift range of the transmission flux of the 30 Keck QSO absorption spectra.

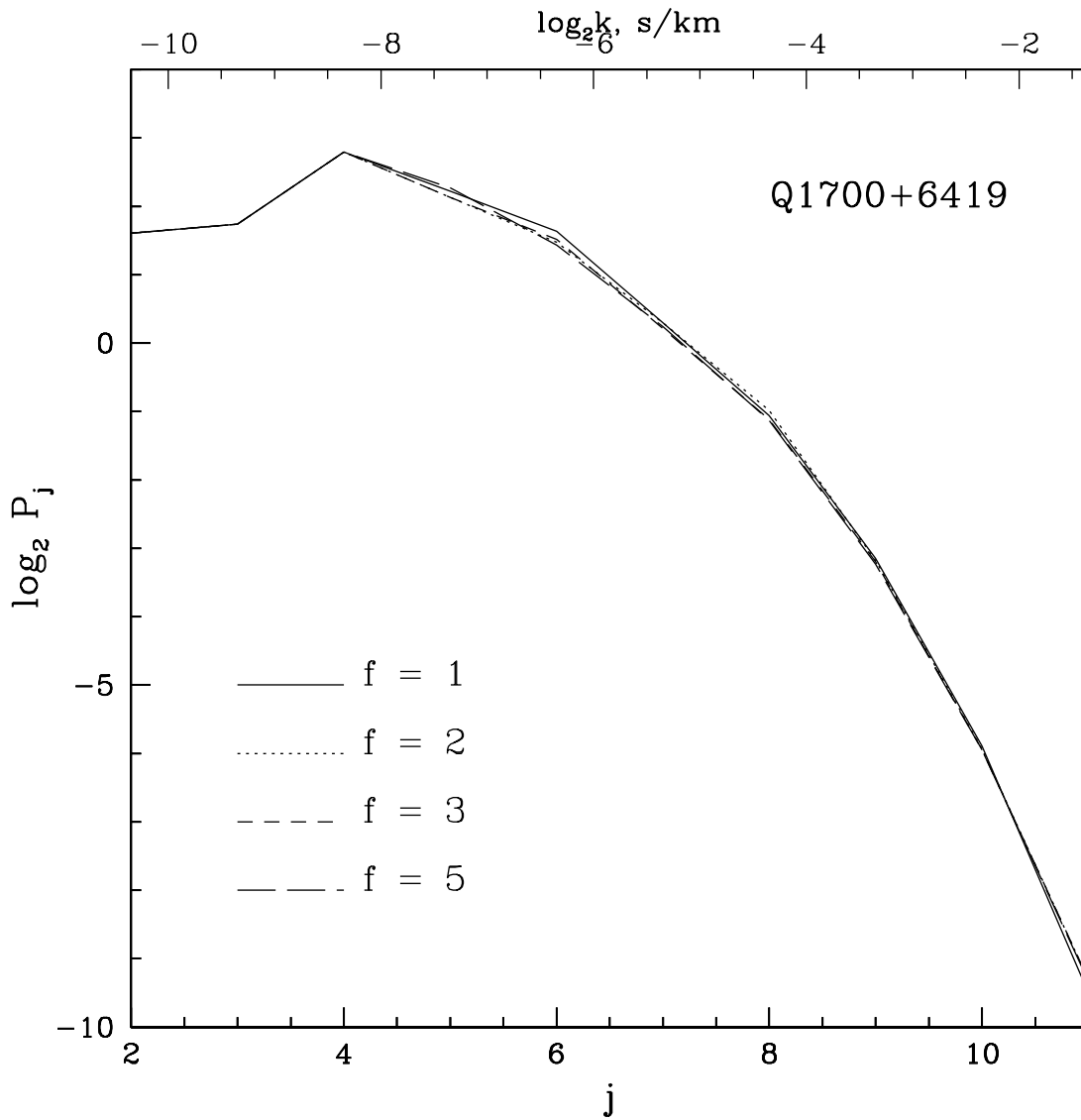


Figure 2: The DWT power spectra  $P_j$  of Q1700+6419. The parameter  $f$  for the conditional counting is taken to be 1, 2, 3 and 5. From §4.1, the scale  $j$  corresponds to  $\Delta\nu = 2c\{1 - \exp[-(1/2)2^{13-j}\delta\nu/c]\} \simeq 2^{13-j}\delta\nu$ , and  $k = 2\pi/2^{13-j}\delta\nu$  s/km.



Q1103+6416

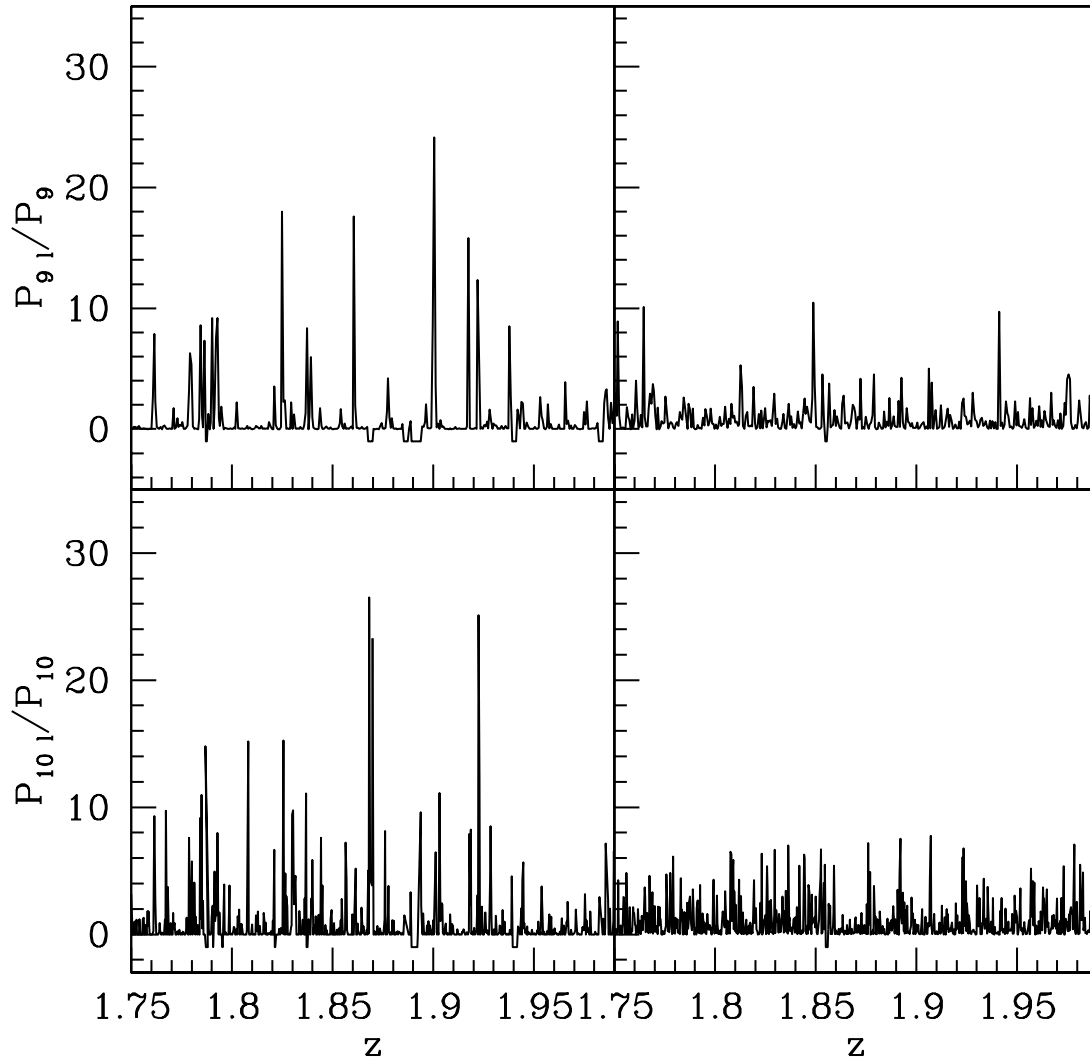


Figure 3: A section of the spatial distribution of local powers,  $P_{jl}/P_j$  on scales  $j = 9$  and  $10$  (corresponding to  $\sim 64$  and  $32$  km/s) for the sample Q1103+6416. The real field is shown in the left panels and the right panels represent the PR field. Large spikes associated with metal lines have been removed.

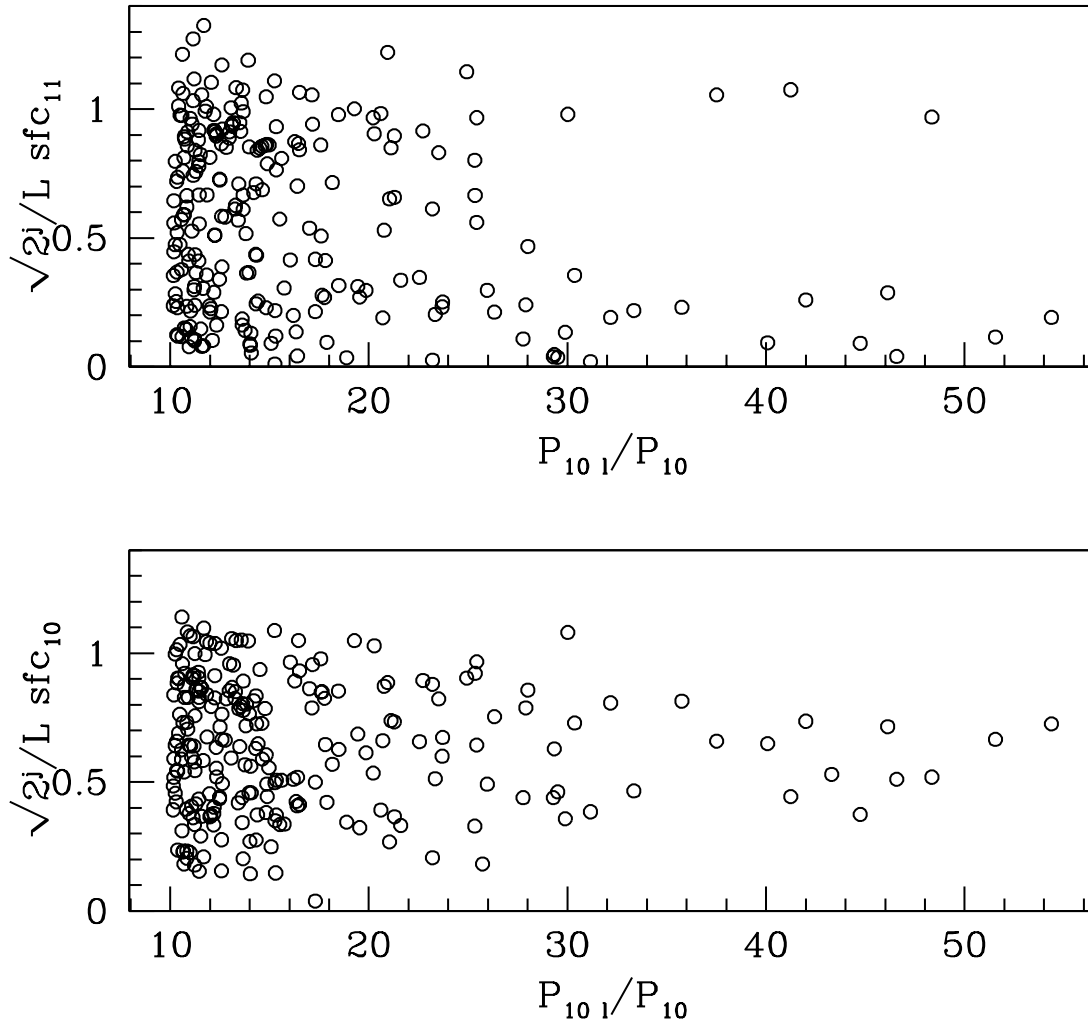


Figure 4: The top 1% local powers on scale  $j = 10$  and their corresponding smoothed fluxes (SFCs) on scales  $j = 11$  (top panel) and 10 (bottom panel).

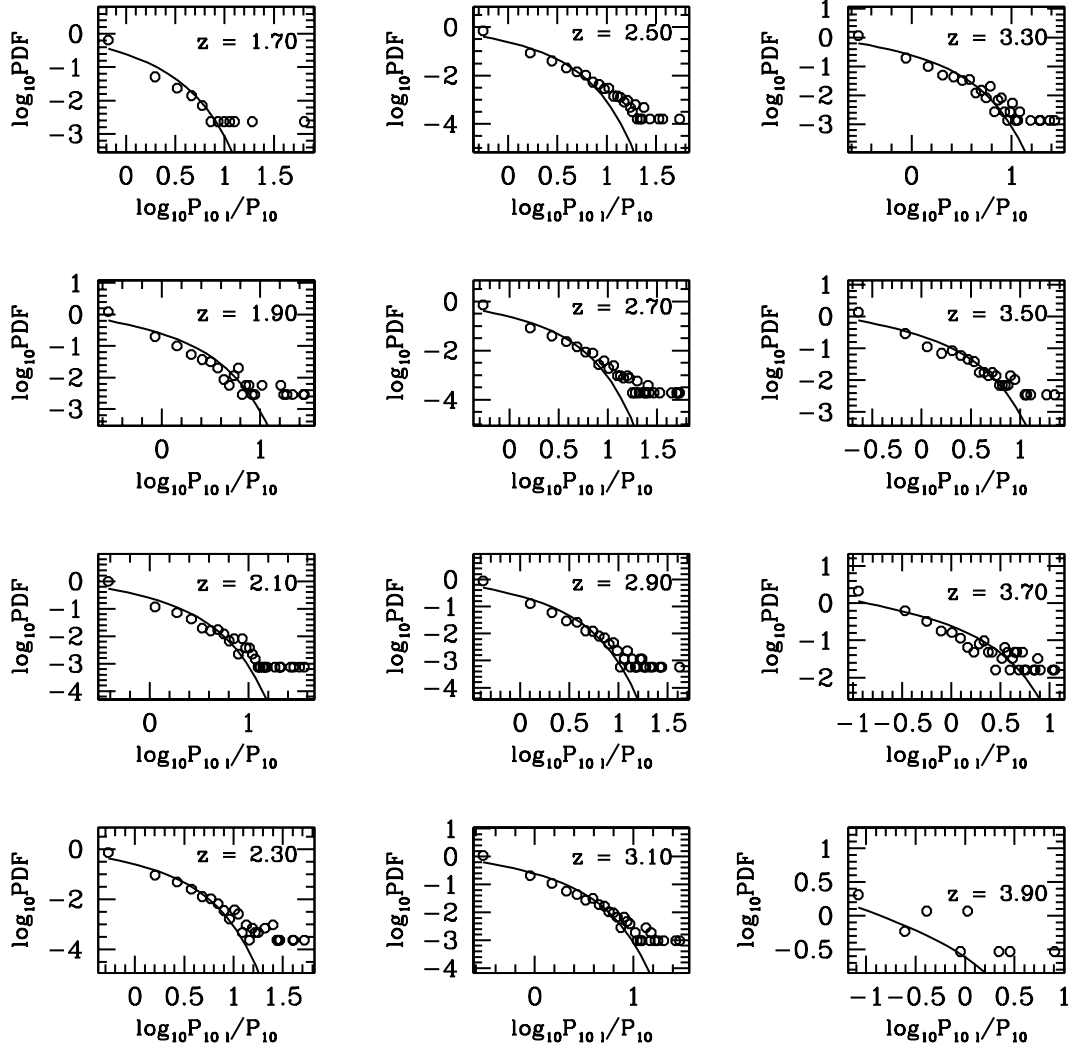


Figure 5: The PDFs of  $P_{j1}/P_j$  of real samples on the scale  $j = 10$  in 12 redshift ranges  $z = 1.6 + n \times 0.2$  to  $1.6 + (n + 1) \times 0.2, n = 0, \dots, 11$ . The solid lines are the  $\chi^2(N = 1)$  distribution.

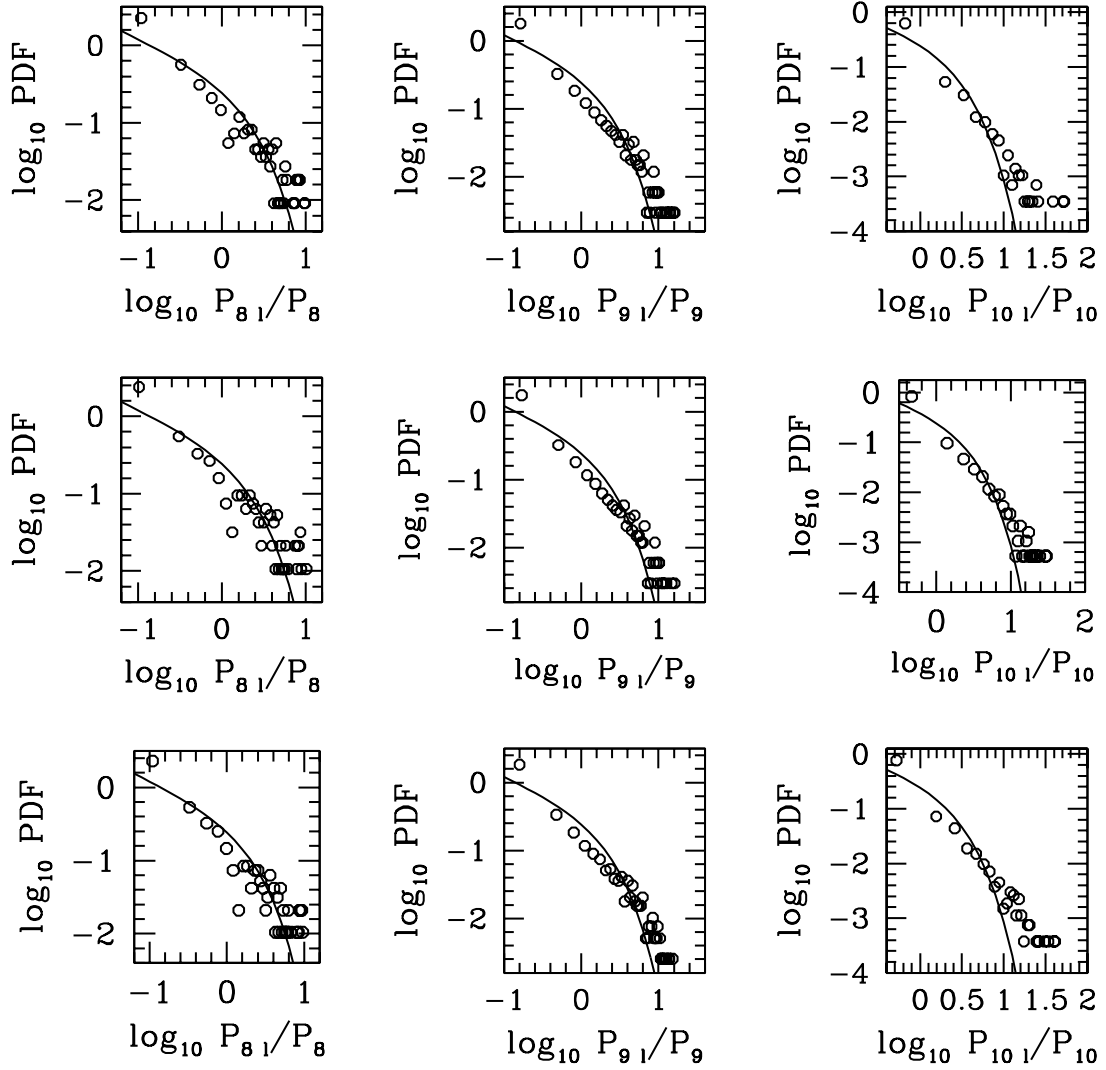


Figure 6: The PDF of  $P_{j1}/P_j$  of real samples on scales  $j = 8, 9$  and  $10$  in redshift range  $z = 2.8$  to  $3.0$ . The parameter  $f$  is taken to be  $1$  (top),  $3$  (middle) and  $5$  (bottom). The solid lines are the  $\chi^2(N = 1)$  distribution.

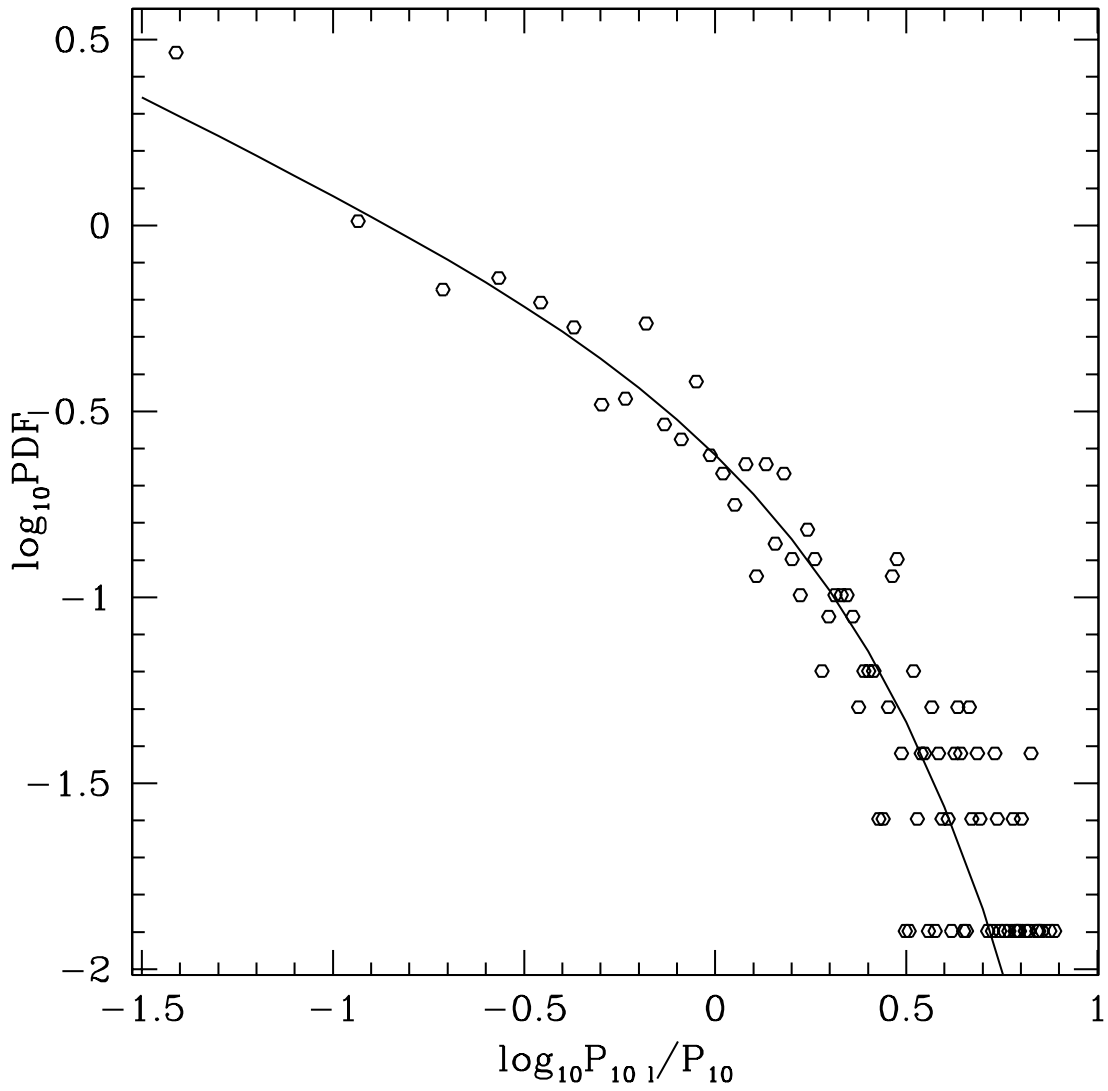


Figure 7: The PDF of  $P_{j1}/P_j$  of the PR sample of Q1103+6416 on scales  $j = 10$ . The solid line is the  $\chi^2(N = 1)$  distribution.

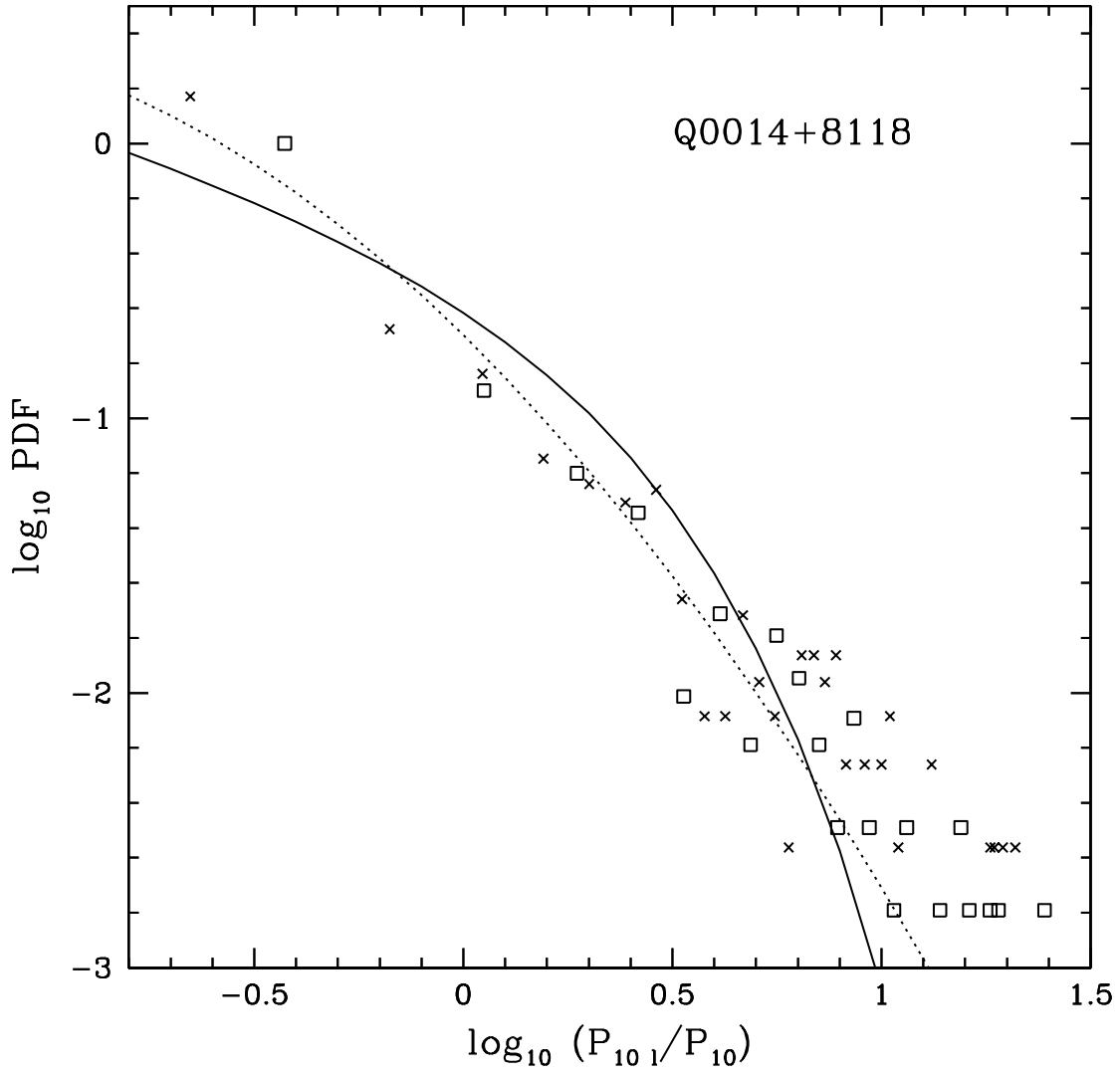


Figure 8: The PDF of  $P_{j1}/P_j$  for Q0014+8118 and  $f = 3$  without the removal of metal lines (squares), and with the removal of metal lines and metal line suspects from the big spikes (crosses). The solid line is the  $\chi^2(N = 1)$  distribution. The dotted line is the lognormal distribution (eq. (26)) with  $\mu = 1.5$ .

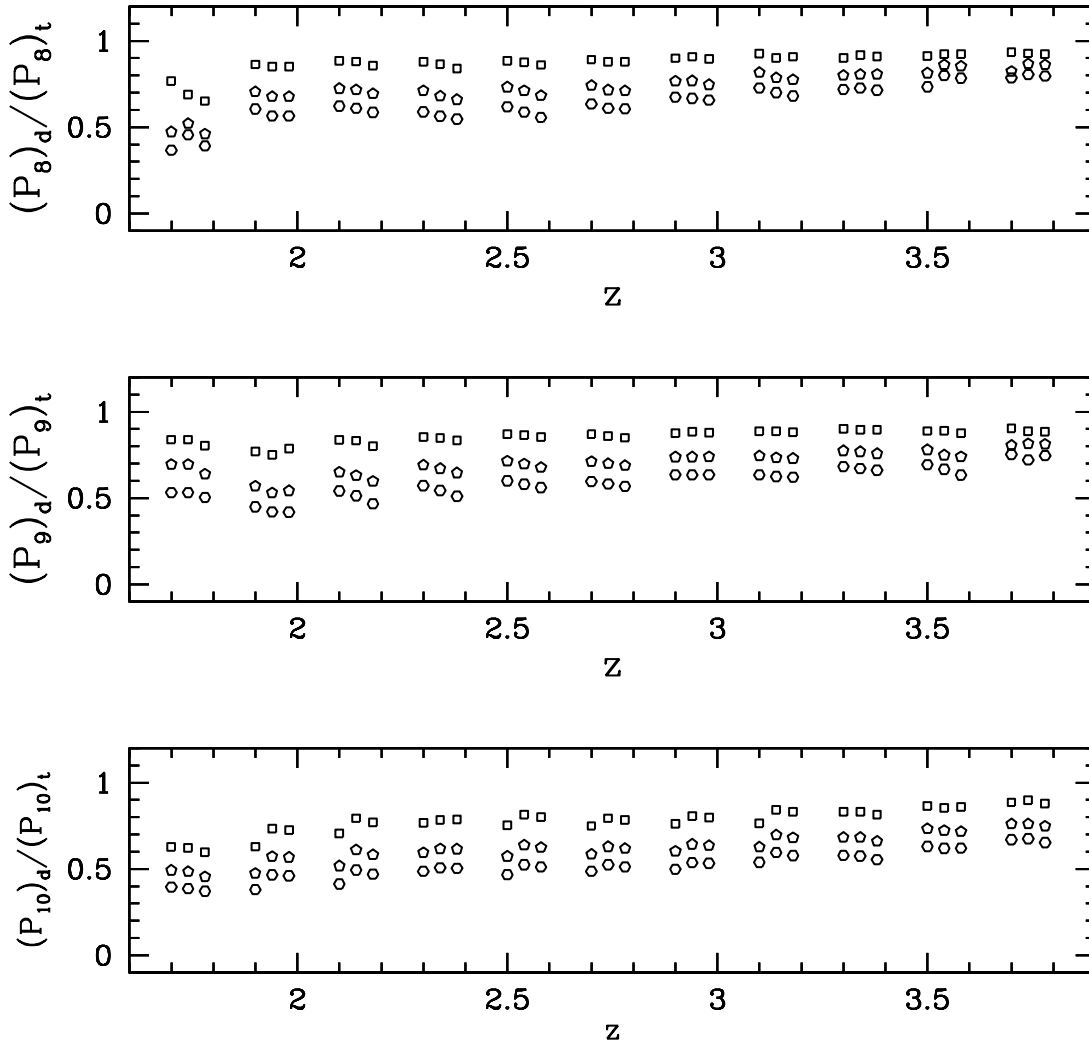


Figure 9: Ratio of power  $(P_{jl})_d$  with top modes dropped to the total power vs. redshift of real data on scales  $j = 8, 9$  and  $10$ . Square, pentagon and hexagon are, respectively, the ratio of powers when the top 1%, 3% and 5% data are dropped.

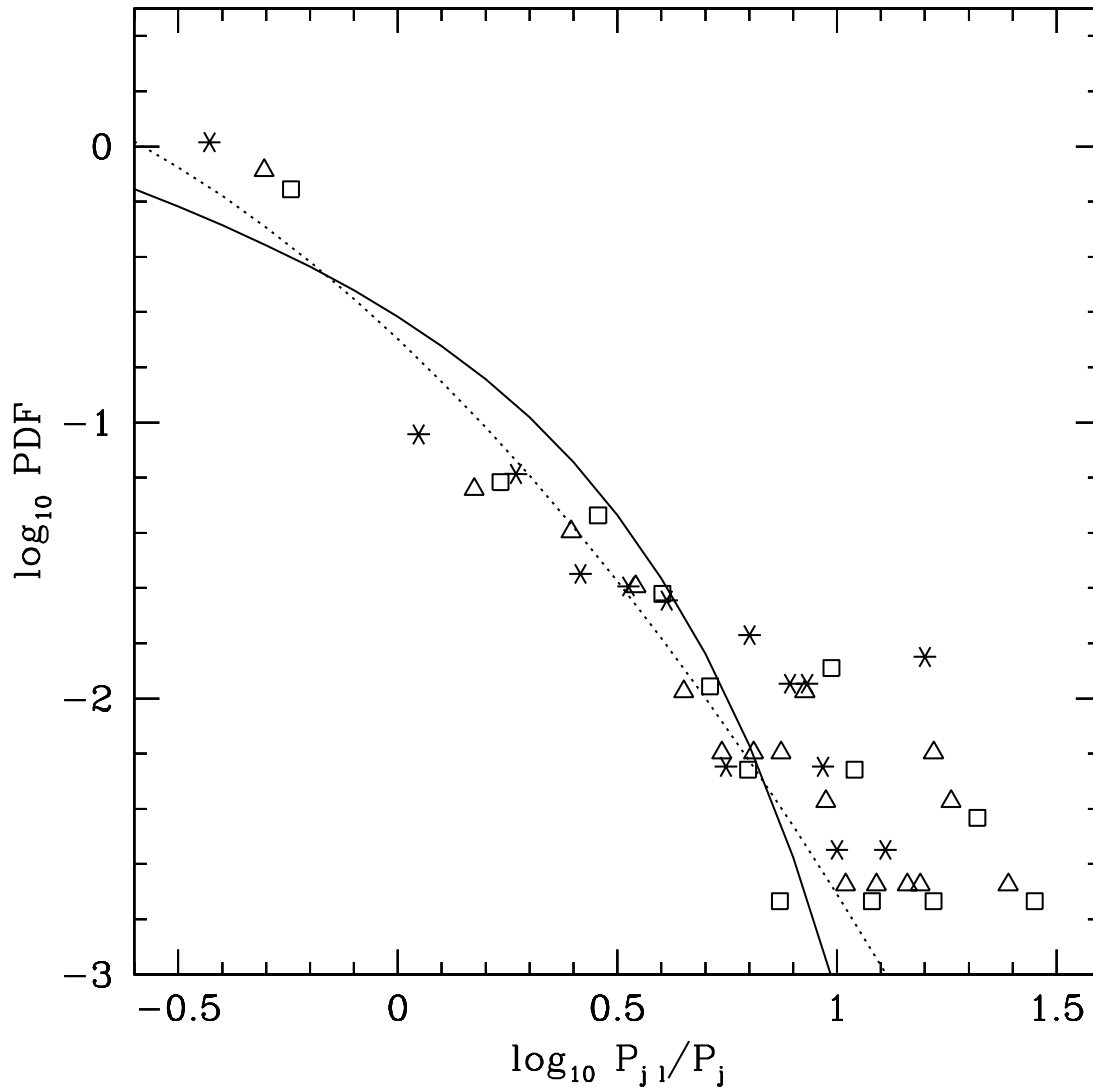


Figure 10: The PDF of  $P_{j1}/P_j$  for Q1103 on scale  $j = 9$ . Triangles are for real data. Squares and crosses correspond to two bootstrap realizations. The solid line is the  $\chi^2(N = 1)$  distribution. The dotted line is the lognormal distribution (eq. (26)) with  $\mu = 1.5$ .



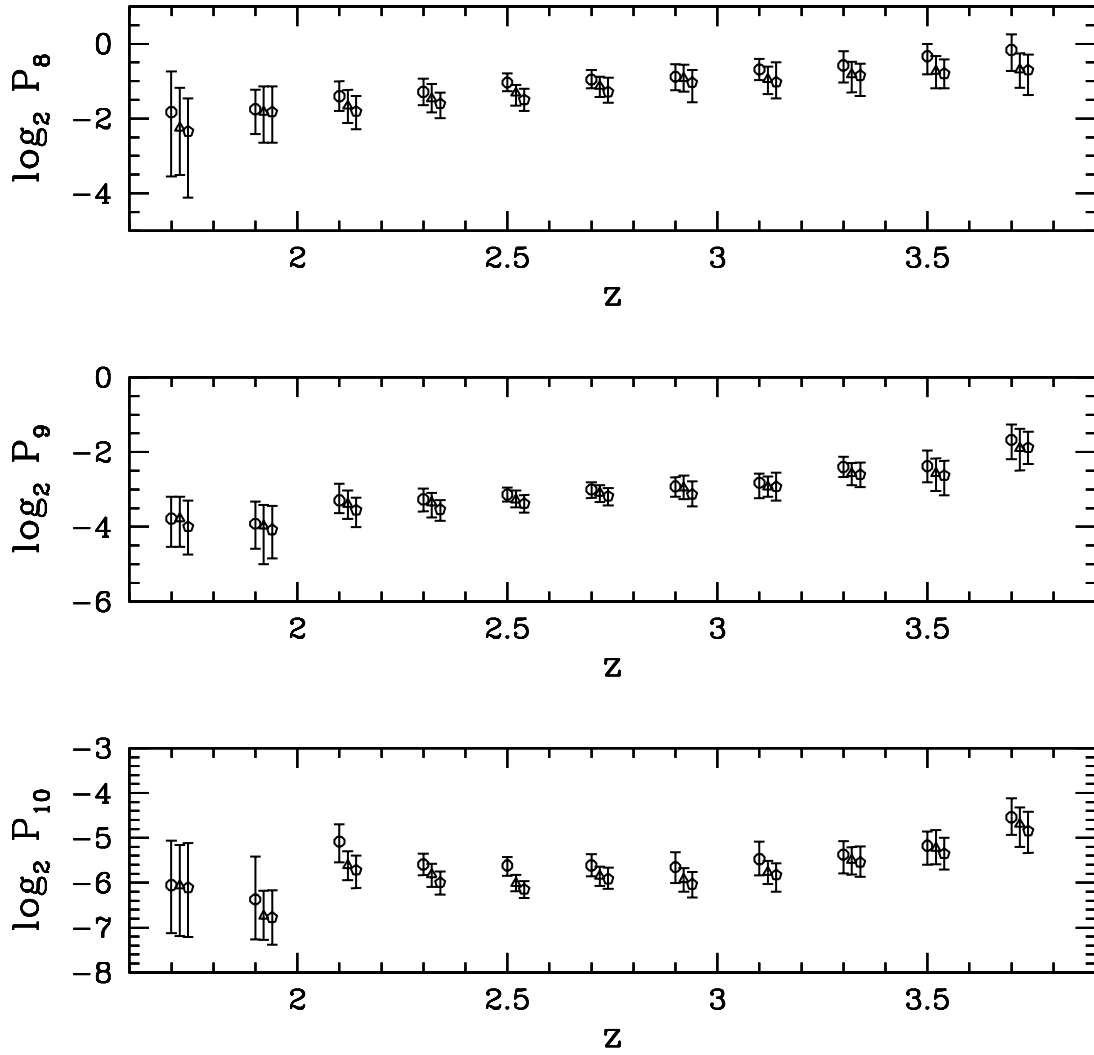


Figure 11: The power spectrum,  $P_j$  on scales  $j = 8, 9$  and  $10$ , in each redshift bin of the Keck data. Error bars are the 99% confidence given by the bootstrap resampling. The parameter  $f$  is taken to be 1 (circle), 3 (triangle) and 5 (pentagon).